

Freeform shape optimization of a compact DC photo-electron gun using isogeometric analysis

Peter Förster* and Sebastian Schöps

*Institute for Accelerator Science and Electromagnetic Fields,
Technische Universität Darmstadt, Schloßgartenstraße 8, 64289 Darmstadt, Germany*

Joachim Enders and Maximilian Herbert

*Institut für Kernphysik, Fachbereich Physik, Technische Universität Darmstadt,
Schloßgartenstraße 9, 64289 Darmstadt, Germany*

Abele Simona

*Laboratory for Modeling and Scientific Computing,
Politecnico Milano, p.za Leonardo da Vinci 32, 20133 Milano, Italy*

Compact DC high-voltage photo-electron guns are able to meet the sophisticated demands of high-current applications such as energy-recovery linacs. A main design parameter for such sources is the electric field strength, which depends on the electrode geometry and is limited by the field-emission threshold of the electrode material. In order to minimize the maximum field strength for optimal gun operation, isogeometric analysis (IGA) can be used to exploit the axisymmetric geometry and describe its cross section by non-uniform rational B-splines, the control points of which are the parameters to be optimized. This computationally efficient method is capable of describing CAD-generated geometries using open source software (GEOPDES, NLOPT, OCTAVE) and it can simplify the step from design to simulation. We will present the mathematical formulation, the software workflow and the results of an IGA-based shape optimization for a planned high-voltage upgrade of the DC photogun teststand Photo-CATCH at TU Darmstadt. The software builds on a general framework for isogeometric analysis and allows for easy adaptations to other geometries or quantities of interest. Simulations assuming a bias voltage of -300 kV yielded maximum field gradients of 9.06 MV m^{-1} on the surface of an inverted-insulator electrode and below 3 MV m^{-1} on the surface of the photocathode.

Keywords: electron gun, shape optimization, finite elements, splines

I. INTRODUCTION

Advanced applications of electron accelerators, for example, energy-recovery linacs (ERLs, [1, 2]), require beams with high current and small emittance, therefore placing sophisticated demands on electron sources. State-of-the-art DC high-voltage photo-electron guns are promising candidates for meeting these requirements [3, 4]. The electrostatic design for this type of source, in light of optimizing the beam properties, has been discussed for many decades [5, 6]. [For example, there exists extensive research focused on the optimization of beam parameters depending on electron bunch parameters \[7\].](#) For instance, the electrode geometry was optimized for gun performance in [8], using a set of parameters that describe a few key geometric features. In contrast, this paper is dedicated to freeform optimizing the shape of the electrode in order to minimize field emission, which still represents a major design problem depending on the [specific geometry of the setup](#). Low-level field emission can have a significant negative impact on the vacuum conditions within the gun and may severely degrade beam quality and operational lifetime [9]. High-level field emis-

sion can cause extensive damage to both electrode and insulator, necessitating repair or even replacement of the components. However, a high bias voltage is desired to provide sufficient initial acceleration for the beam and to minimize emittance in spite of space-charge effects. Since common negative bias voltages of state-of-the-art DC photo-electron guns are in the range of -100 kV to -500 kV [10–13], the combination of such high voltages with a suitable electrode geometry and material poses a great challenge for the design of compact guns. The decisive limiting factor is the field emission threshold of the electrode material, imposing a maximum electric field strength on the geometric design. While increasing the curvature of the electrode surface reduces the field maximum, the overall size of the electrode is limited since the surface area susceptible to field emission should be kept small. Furthermore, a larger electrode requires a larger vacuum chamber, which can be impractical due to cost and space constraints. A promising approach is the so-called inverted-insulator geometry gun (IIGG) design [10, 14], which significantly reduces the size of the electrode by placing the high-voltage insulator inside the vacuum chamber.

Practical experience shows that unavoidable material impurities and limitations in machining may cause significant variations in the field emission threshold. It is therefore paramount to keep the maximum electric field

* peter.foerster@cem.temf.de

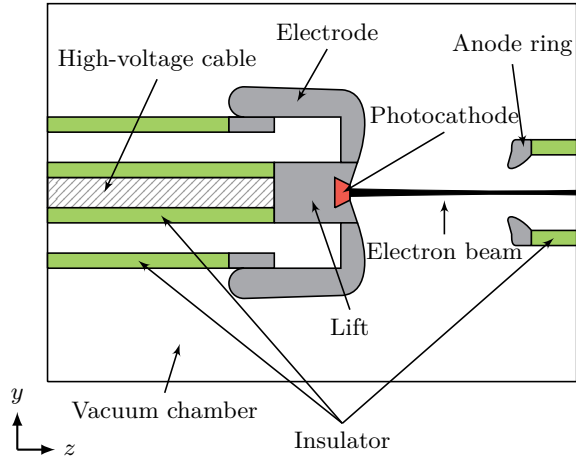


Figure 1: Basic components of the IIGG design in a longitudinal cross section of the vacuum chamber.

strength of the design well below the threshold. For stainless steel (1.4429 ESU), a commonly used electrode material, the threshold estimate from operational observations is 10 MV m^{-1} [15]. Other available materials, such as niobium, titanium, and molybdenum possess a higher threshold for field emission [16, 17], but are more expensive and more difficult to machine. Common electrode designs range from simple spherical and cylindrical forms to more complex geometries like the T-shaped design used at JLab [14].

At TU Darmstadt, a test facility for Photo-Cathode Activation, Test, and Cleaning using atomic-Hydrogen, Photo-CATCH, which is also dedicated to DC photoelectron gun research and development, has been established recently [18]. It uses an axisymmetric IIGG, featuring a two-part electrode consisting of a main electrode body and an extendable lift for photocathode loading [19]. An upgrade from -60 kV to -300 kV bias voltage has been envisioned and is currently under development. In order to meet design constraints concerning available space and chamber size, an adaptation and optimization of the existing geometry is necessary. The important components of the planned design are shown in Figure 1.

A key limitation of the design optimization process is the manual input and adaption of shapes based on simulations that must be repeated accordingly. An automation of these steps is desired in order to accelerate and simplify the design process. This leads to numerical shape optimization. Since the spatial description of the electric field inside the gun follows (the electrostatic approximation of) Maxwell’s partial differential equations (PDEs), the shape optimization problem is PDE-constrained [20]. Furthermore, there commonly is no closed-form solution available for complex geometries, so the PDE is solved numerically, for example, by finite elements [21].

PDE-constrained optimization is well known in the

computational electromagnetics community, see the textbook [22] and the references therein. Particularly in the context of electron guns, several design workflows to optimize their geometry have been proposed in the last decades [23–27]. However, all of them belong to the class of parameter-based optimization, i.e., the designer has to create a template which contains the design variables describing the geometry, e.g., width, height, and radius. This restricts the design space and is an inconvenient manual effort. On the other hand, computer aided design (CAD) tools allow freeform shapes in terms of splines and non-uniform rational basis splines (NURBS) [28, 29]. Numerical shape optimization uses the parameters of these NURBS as the degrees of freedom (DOFs) and thus allows for an improved balance between design freedom and ease of implementation. Both parameter and shape optimization may also be used to describe the shape and position of holes in the geometry, however neither is able to introduce new ones. This requires a further generalization and leads to topology optimization, but this is not of interest in the context of our application. An illustration of the different types of geometric design optimization is given in Figure 2.

There is another important difference between our method and previous workflows. Each geometry realization is discretized separately in the approaches cited above, which requires rather fine spatial resolutions to avoid numerical errors due to remeshing (‘mesh noise’) and may again require additional manual intervention. According to Sandia Labs, about 75 % of the simulation time in research laboratories is spent on modeling, parameterization, mesh generation, as well as pre- and post-processing [30]. Yet another distinction should be made regarding the quality of the resulting field solutions. The current state of the art in the accelerator community are low order finite element codes, e.g., POISSON [31]. However, even higher-order classical finite element codes, e.g., CST [32], yield noisy fields due to the lack of global regularity, see [33, Figure 4]. This is cumbersome for particle tracking and either needs smoothing or dedicated (symmetry-preserving, mixed element) meshing. To this end, this paper proposes a spline-based shape optimization workflow using isogeometric analy-

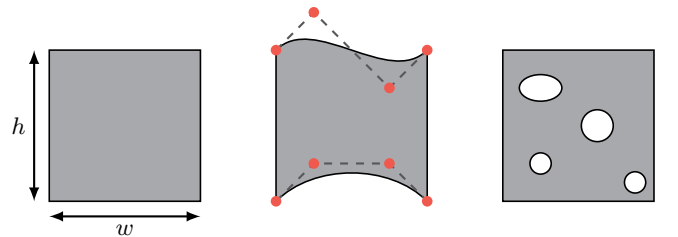


Figure 2: Different types of design optimization. From left to right: parameter, shape, and topology optimization.

sis (IGA) [34], which integrates finite element analysis into the conventional NURBS-based CAD design workflow and allows for integrated particle tracking. IGA-based optimization is well established in many communities, but less explored in electromagnetism. However, [35, 36] applied IGA-based optimization to accelerator magnets (without tracking), and more recently [37] suggested a freeform-optimization workflow based on shape calculus for rotating electric machines; more references can be found in the survey article [38].

The paper is structured as follows: after this introduction, section II gives a short summary on CAD geometry handling and introduces splines. The following section III introduces the electric field problem, its weak formulation, discretization, and particle tracking. Then section IV formulates the optimization problem and introduces numerical methods for its solution and section V discusses the results for the particular gun in the context of Photo-CATCH. Finally, the paper closes with conclusions and an outlook.

II. SPLINES AND GEOMETRY

CAD models are essentially represented by B-splines [28] and NURBS [39], since they can exactly describe circular objects, allow local smoothness control, and give an intuitive definition of freeform curves and surfaces by so-called control points [40].

A. B-splines

A basis $\{B_{i,p}\}_{i=1}^{N_{\text{dim}}}$ of a one-dimensional B-spline space \mathbb{S}_α^p of degree p and regularity α may be constructed from a knot vector $\Xi = (\xi_1, \xi_2, \dots, \xi_n) \in [0, 1]^n$, $\xi_1 \leq \xi_2 \leq \dots \leq \xi_n$ using the Cox-de Boor algorithm [41]

$$B_{i,0}(\xi) = \begin{cases} 1 & \text{if } \xi_i \leq \xi < \xi_{i+1} \\ 0 & \text{otherwise} \end{cases}$$

$$B_{i,p}(\xi) = \frac{\xi - \xi_i}{\xi_{i+p} - \xi_i} B_{i,p-1}(\xi) + \frac{\xi_{i+p+1} - \xi}{\xi_{i+p+1} - \xi_{i+1}} B_{i+1,p-1}(\xi).$$

The knot vector uniquely determines the basis and its properties, for example, smoothness and the like. The knots do not need to be unique and the multiplicity m_j of a knot value ξ_j , $1 \leq j \leq n$ determines the continuity of the basis in that knot to be C^{p-m_j} . Furthermore, a knot vector is said to be open if its first and last knots have multiplicity $p+1$. For geometry modeling this usually is the case, since it makes the curve interpolatory in the first and last knot. It also leads to a distinction between the first, last, and the internal knots. The latter influence the shape of the basis splines, as they represent the interfaces between each of the polynomial pieces (or elements) that make up the splines.

B. Geometry description

Given a set of control points $\{\mathbf{P}_i\}_{i=1}^{N_{\text{dim}}} \subset \mathbb{R}^2$, a two-dimensional (bivariate) B-spline curve is described by a linear combination of the basis functions

$$C_{\mathbf{P}}(\xi) = \sum_{i=1}^{N_{\text{dim}}} \mathbf{P}_i B_{i,p}(\xi). \quad (1)$$

This representation is convenient for shape optimization for multiple reasons. For one, the uniqueness of the basis for a given knot vector leads to an interpretation of the control points as giving the curve its shape. As a consequence, changes in the coordinates of the control points directly translate to changes in the shape of the curve and most importantly they do so smoothly. An exemplary curve along with the corresponding basis is shown in Figure 3a. The extension of (1) to the two-dimensional case follows from choosing bases $\{B_{i,p_1}\}_{i=1}^{N_1}$, $\{B_{j,p_2}\}_{j=1}^{N_2}$ of $\mathbb{S}_{\alpha_1, \alpha_2}^{p_1, p_2}$ and a control mesh, given by an ordered set of $N_1 \times N_2$ control points $\mathbf{P}_{i,j}$. A B-spline surface $S_{\mathbf{P}}$ is then defined similarly to the one-dimensional case via

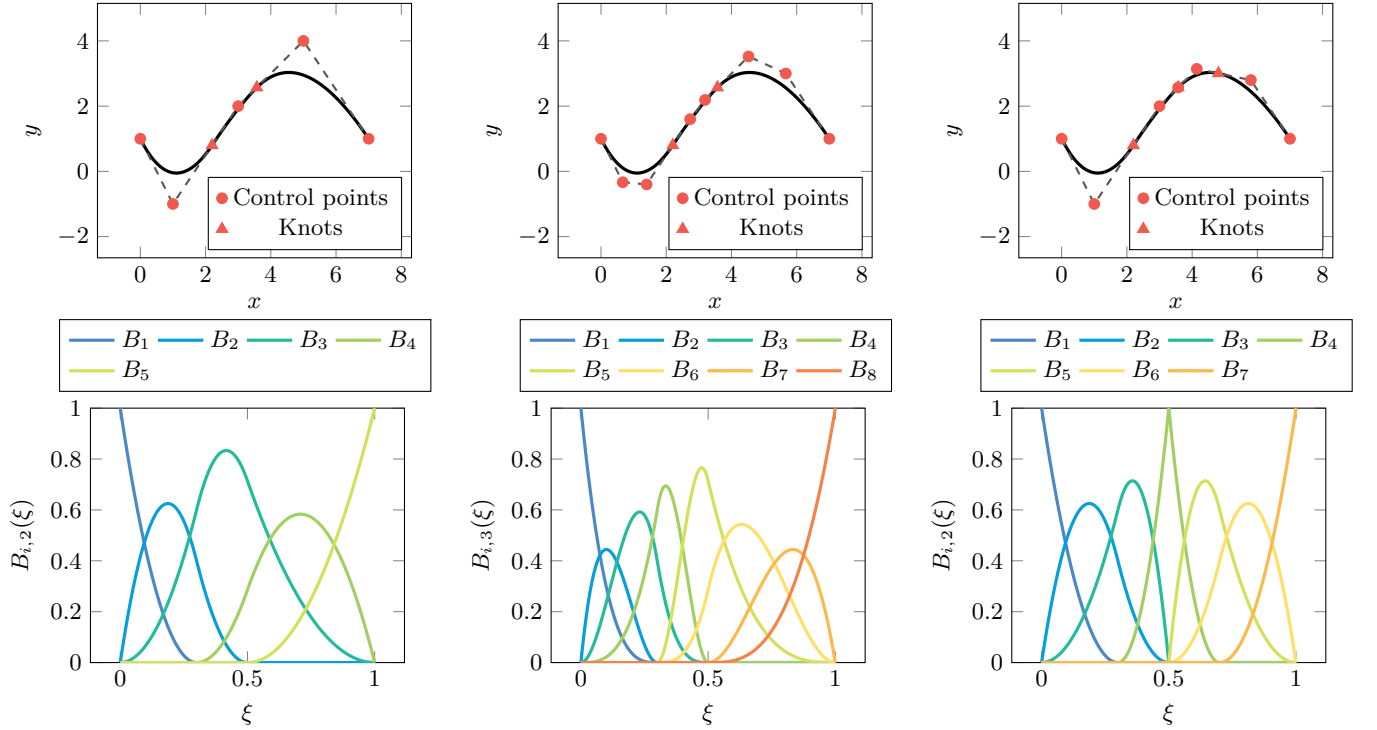
$$S_{\mathbf{P}} = \sum_{i=1}^{N_1} \sum_{j=1}^{N_2} \mathbf{P}_{i,j} B_{i,p_1} B_{j,p_2}$$

and also volumetric (trivariate) mappings $V_{\mathbf{P}}$ can be defined analogously. For the construction and handling of the bi- and trivariate geometry descriptions we make use of the free NURBS package [42].

C. Refinement

There are several approaches to refine an existing B-spline basis $\{B_{i,p}\}_{i=1}^{N_{\text{dim}}}$. One is degree elevation, whereby the polynomial degree p of the basis functions is increased. In order for the continuity of the original curve to be preserved, the multiplicity of each knot ends up being increased alongside the degree. Furthermore each element, i.e., each polynomial piece, gains new control points equal to the increase in degree and the positions of all control points are recomputed such that the shape and parameterization of the curve are maintained. Figure 3b shows an example of the process.

A second refinement strategy is given by knot insertion. Here, an arbitrary internal knot is added to the knot vector. This does not impact the degree of the basis, however the total number of basis functions is still increased and the continuity of the basis in the new knot is reduced. For each inserted knot, a new control point is added as well and again the positions of all control points are determined in a way to keep the shape of the curve intact. An illustration of the process is given in Figure 3c. Note that after inserting a knot at 0.5 the basis becomes C^0 continuous in that point, as expected. For a more comprehensive treatment of the geometry descriptions and refinement strategies we refer to [34].



(a) Original curve and basis functions.

(b) Curve and basis functions after elevating the degree by 1.

(c) Curve and basis functions after inserting knots at 0.5 and 0.7.

Figure 3: Exemplary B-spline curves and their basis functions. The original knot vector is $\Xi = (\mathbf{0}_{1 \times 3}, 0.3, 0.5, \mathbf{1}_{1 \times 3})$ and the control points are $\mathbf{P}_1 = (0, 1)$, $\mathbf{P}_2 = (1, -1)$, $\mathbf{P}_3 = (3, 2)$, $\mathbf{P}_4 = (5, 4)$ and $\mathbf{P}_5 = (7, 1)$.

III. FIELD FORMULATION AND DISCRETIZATION

Let Ω be the computational domain of the electron gun with boundary $\partial\Omega$. In the absence of space charges, the electric field strength $\mathbf{E} = \mathbf{E}(\mathbf{x})$, $\mathbf{x} \in \Omega$ within the gun is described by the electrostatic subset of Maxwell's equations [43]

$$\nabla \times \mathbf{E} = 0 \quad \text{and} \quad \nabla \cdot (\varepsilon \mathbf{E}) = 0$$

in Ω , where the permittivity is given by

$$\varepsilon = \begin{cases} \varepsilon_{\text{ins}} & \text{in } \Omega_{\text{ins}} \\ \varepsilon_0 & \text{otherwise,} \end{cases}$$

compare Figure 4, where ε_0 and ε_{ins} are the permittivities of empty space and the insulator, respectively. We assume that the domain is given by a multipatch spline mapping from the reference domain $\hat{\Omega} = (0, 1)^3$ to the physical domain, that is, $\Omega = \Omega(\mathbf{P})$ in terms of control points \mathbf{P} , see [44]. Introducing the electric scalar potential ϕ by $\mathbf{E} = -\nabla\phi$ yields the boundary value problem [43, Section 1.7]

$$\nabla \cdot (\varepsilon \nabla \phi) = 0 \quad \text{in } \Omega, \quad (2)$$

along with the Dirichlet boundary conditions $\phi = \phi_{D_i}$ on Γ_{D_i} ($i = 1, 2, 3$), see Figure 4.

A. Weak formulation

Exploiting the axisymmetry of the configuration we may restrict our analysis to Ω^{2D} , i.e., the ρ - z -plane. Let $V = H^1(\Omega^{2D})$ denote the space of square-integrable functions with square-integrable gradients [21]. Following the Ritz-Galerkin approach, we deduce the weak form of (2) as: find $\phi \in V_D$ such that

$$\int_{\Omega^{2D}} \varepsilon \nabla \phi \cdot \nabla \phi' \, \rho \, d\rho \, dz = 0, \quad (3)$$

for every $\phi' \in V_0$, where V_D indicates the space of functions in V satisfying the Dirichlet boundary conditions, while V_0 indicates the V subspace of functions vanishing on Γ_D . A finite-element-like discretization of (3) is obtained by restricting to a finite-dimensional subspace $V_h \subset V$. Using basis functions $\{v_i\}_{i=1}^N$ of V_h allows to express the potential as

$$\phi_h = \sum_{i=1}^N \varphi_i v_i, \quad \varphi_i \in \mathbb{R} \quad (4)$$

and the approximated electric field strength follows from $\mathbf{E}_h = -\nabla\phi_h$. The linear system of equations reads

$$\mathbf{K}_\varepsilon \boldsymbol{\varphi} = -\boldsymbol{\varrho}, \quad (5)$$

where we consider only the N_{dof} unconstrained coefficients as degrees of freedom, i.e.,

$$(\mathbf{K}_\varepsilon)_{ij} = \int_{\Omega^{2D}} \varepsilon \nabla v_j \cdot \nabla v_i \rho \, d\rho \, dz \quad (6)$$

for $1 \leq i, j \leq N_{\text{dof}}$ and include the coefficients known due to boundary conditions in the right-hand-side $\boldsymbol{\varrho}$.

Please note, until now the basis functions have not yet been specified. The next section will propose to use B-splines instead of the more common finite-element-type hat functions [34].

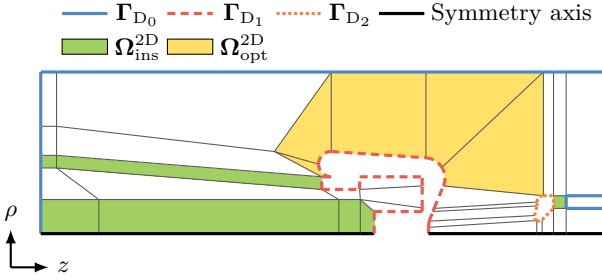


Figure 4: Original geometry and boundary conditions of the domain Ω^{2D} . Grey lines indicate patch boundaries.

B. Isogeometric analysis

The main idea of IGA is to use B-splines or NURBS not only for the geometry description but also to represent the solution. This allows to solve numerical problems, as the one defined above, on computational domains without introducing a geometric modeling error. Moreover, the thereby obtained geometry parameterization lends itself very nicely towards shape optimization, since it offers an intuitive set of degrees of freedom which immediately deform the underlying mesh. Finally, the usage of high-order B-spline basis functions in (5) guarantees rapid convergence and a high continuity of the solution [34].

Let $S_{\mathbf{P}} : \hat{\Omega}^{2D} \rightarrow \Omega^{2D}$ denote the bivariate geometry mapping from the reference domain $\hat{\Omega}^{2D} := (0, 1)^2$ to the physical domain, from which eventually a 3D description is obtained by revolution [45]. Assuming that $S_{\mathbf{P}}$ is piecewise smoothly invertible, we may define the approximation space V_h using a gradient preserving transformation

$$V_h = \{v : v = \hat{v} \circ S_{\mathbf{P}}^{-1}, \hat{v} \in \hat{V}_h\}.$$

Here \hat{V}_h is a discrete space on the parametric domain, for which we elect to use the space of B-splines with degree p_i and continuity α_i along dimension i , denoted by

$\mathbb{S}_{\alpha_1, \alpha_2}^{p_1, p_2}$ in the presented two-dimensional case. We have implemented the weak form and the discretization by IGA within the free software GEOPDES [46].

C. Particle tracking

Having determined the electric field, particle tracking can be performed which profits from the high continuity of the numerically computed field \mathbf{E}_h . Even if the tracking tool only supports point-wise data import; this is, for example, the case for ASTRA [47], regularity can be reconstructed if high-order interpolation is used. ASTRA can make use of higher order polynomial interpolation internally, such that fields and first derivatives with respect to the space coordinates are continuous functions, for example, when computing space charge effects [47, Sections 4.3, 4.4 and 6.9].

The tracking aims at solving the equations of motion of the particles

$$\frac{d\mathbf{x}}{dt} = \mathbf{v} \quad \text{and} \quad \frac{d\mathbf{p}}{dt} = q(\mathbf{E}_h + \mathbf{v} \times \mathbf{B}_h) \quad (7)$$

for given initial conditions. Here, $\mathbf{x} = \mathbf{x}(t)$ denotes the position of a single particle as a function of time, \mathbf{v} , \mathbf{p} its velocity and momentum respectively and q its charge. For the considered problem there exists no contribution from a magnetic field, so $\mathbf{B}_h = 0$. The electric field however is made up of two components: an external part described by $\mathbf{E}_h = -\nabla\phi_h$ from (4), and an internal one originating from the space charge forces due to the particles themselves. Various approaches exist for the numerical treatment, e.g., time integration, see [48–51] and references therein.

Once the particle trajectories are computed, it is possible to evaluate statistical quantities that give insight into the gun's performance. Two of these quantities of interest (QoI) are the root mean square (rms) beam width $\mathbf{x}_{\text{rms}} \in \mathbb{R}^{N_z}$ and the related normalized transverse rms emittance $\epsilon_x \in \mathbb{R}^{N_z}$, both in the x - and y -direction, where N_z is the number of discrete points along the z -axis where the trajectories are known. Let $\mathbf{X} \in \mathbb{R}^{N_p \times N_z}$ be a matrix containing the x -coordinates of the N_p particles, and similarly we denote by $\mathbf{P}_x \in \mathbb{R}^{N_p \times N_z}$ a matrix containing the x -components of their momenta. The j^{th} entries of the QoI in the x -direction can then be determined via

$$(\mathbf{x}_{\text{rms}})_j = \sqrt{\frac{\sum_{i=1}^{N_p} (\mathbf{X})_{ij}^2}{N_p} - \left(\frac{\sum_{i=1}^{N_p} (\mathbf{X})_{ij}}{N_p} \right)^2} \quad (8)$$

$$(\epsilon_x)_j = \frac{\pi}{mc_0} \sqrt{(\mathbf{x}_{\text{rms}})_j^2 (\mathbf{p}_{\text{rms}})_j^2 - (\mathbf{r}_{xp})_j^2} \quad (9)$$

where

$$(\mathbf{p}_{\text{rms}})_j = \sqrt{\frac{\sum_{i=1}^{N_p} (\mathbf{p}_x)_{ij}^2}{N_p} - \left(\frac{\sum_{i=1}^{N_p} (\mathbf{p}_x)_{ij}}{N_p} \right)^2}$$

$$(\mathbf{r}_{xp})_j = \frac{\sum_{i=1}^{N_p} (\mathbf{x})_{ij} (\mathbf{p}_x)_{ij}}{N_p} - \frac{\sum_{i=1}^{N_p} (\mathbf{x})_{ij} \sum_{i=1}^{N_p} (\mathbf{p}_x)_{ij}}{N_p^2}$$

and m , c_0 denote the particle mass and the speed of light in vacuum respectively [52]. The quantities in the y -direction are defined analogously.

For the simulations the well-established particle tracking software ASTRA [47] is used. It offers the possibility to provide the main program with a set of data files containing the electric field values on a pre-defined grid. The initial particle distribution may be given in a similar way, with the positions, momenta, and emission times from the cathode specified in a file. Furthermore, it employs a 4th order non-adaptive Runge-Kutta scheme as the time integrator for the equations of motion of the particles (7). The space charge effects are taken into account by way of a cylindrical grid algorithm that approximates the relativistic effects via a Lorentz transformation to the average rest frame of the bunch. In the presented case of a planar cathode, it is also able to include the mirror charge effects with respect to the cathode plane.

IV. SHAPE OPTIMIZATION

The overall aim is to optimize the geometry of the electron gun to achieve two possibly competing goals. Firstly, we want to minimize the maximum electric field strength on the electrode surface, and secondly, we want to ensure a proper beam.

Only the shape of the electrode is relevant for the geometry, i.e., the boundary Γ_{D_1} in Figure 4. Furthermore, as can be seen in Figure 5b, it makes sense to restrict our attention to the domain Ω_{opt}^{2D} , as indicated in Figure 4. The degrees of freedom for the optimization are given by the positions of the control points \mathbf{P} of the curve $C_{\mathbf{P}}(\rho, z)$ describing that part of Γ_{D_1} , which intersects with Ω_{opt}^{2D} . On a further note, the volume of the electrode may not exceed some fixed value V_c due to space and weight considerations. For this, let $V_{\text{el}}(\mathbf{P})$ denote the volume of the electrode in dependence on $\Gamma_{D_1}(\mathbf{P})$, as characterized in Figure 1.

We allow geometries from an admissible set

$$\mathcal{A} = \{(\mathbf{P}_1, \dots, \mathbf{P}_{N_{\text{opt}}}) : \underline{\mathbf{P}}_i \leq \mathbf{P}_i \leq \bar{\mathbf{P}}_i, i = 1, \dots, N_{\text{opt}}\},$$

where \leq is to be read component-wise. \mathcal{A} accounts for constraints on the coordinates of the control points in terms of upper $\bar{\mathbf{P}}_i$, and lower bounds $\underline{\mathbf{P}}_i$, for example, to avoid intersections. The optimization problem is finally obtained as

$$\min_{\mathbf{P} \in \mathcal{A}} \max_{\mathbf{x} \in \Omega_{\text{opt}}^{2D}(\mathbf{P})} \|\mathbf{E}_h(\mathbf{x}; \mathbf{P})\|_2 \quad (10)$$

subject to

$$\begin{aligned} \mathbf{E}_h(\mathbf{x}; \mathbf{P}) &= -\nabla \phi_h(\mathbf{x}; \mathbf{P}) \quad \text{via (4-5)} \\ V_{\text{el}}(\mathbf{P}) &\leq V_c \\ \mathbf{f}_{\text{track}}(\mathbf{E}_h(\mathbf{x}; \mathbf{P})) &< \text{tol}, \end{aligned} \quad (11)$$

where $\mathbf{x} = (\rho, z)^\top$ is a position in the ρ - z -plane and the inner optimization, $\max \|\mathbf{E}_h(\mathbf{x}; \mathbf{P})\|_2$, is approximated by a discrete maximum over a set of sample points which are used for the numerical quadrature of (6). The function $\mathbf{f}_{\text{track}}$ denotes quantities of interest from the particle tracking, as defined in section III C, and tol describes associated bounds that ensure functionality.

The question of which optimization algorithm to employ for solving the given problem is determined by the lack of smoothness of the min max problem, the unavailability of derivatives, and the nature of the constraints. In this work, we apply a two step process consisting of the successive application of a global, followed by a local, optimization algorithm. The global algorithm (ISRES) is an evolution strategy based on a stochastic ranking to balance the objective function with the constraint based penalty function [53]. *It does not need to compute or estimate derivatives of the objective function and at the same time is able to handle arbitrary nonlinear constraints, thus it meets our requirements. However the associated*

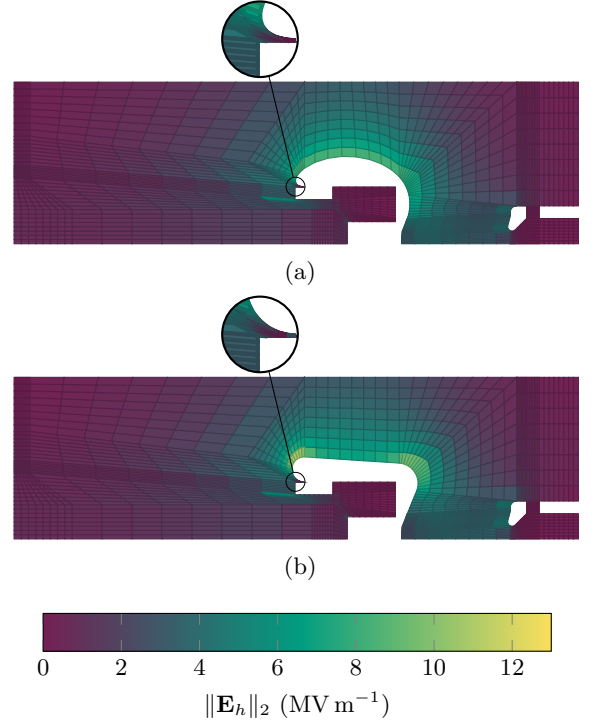


Figure 5: Electric field magnitude for the original (Figure 5b) and optimized (Figure 5a) geometries. The plot representation uniformly divides each patch into 8 elements in each coordinate direction ($n_{\text{sub}} = 8$).

Computed using GEOPDES.

computational effort is comparatively high, as is to be expected with global optimization in general and evolutionary algorithms in particular. The local algorithm (COBYLA) works by creating linear approximations of both the objective and constraint functions via interpolating their evaluations at the vertices of a simplex [54]. This method again meets our criteria of not needing to compute derivatives of the objective function and being able to deal with nonlinear constraints. Even more importantly, the computational cost of this local algorithm is much less compared to that of the global one. We can therefore select smaller tolerances on the change of the objective function over consecutive iterations and still obtain results in a shorter period of time. For either algorithm we make use of the freely available implementations from the NLOPT package [55]. Derivatives, alternative formulations, or approximations of the optimization problem (10) may allow for more sophisticated algorithms. In particular, one may look for a ‘smoother’ objective function that avoids the discrete maximum, or aim for convexity of the optimization problem.

V. NUMERICAL RESULTS

Based on the abstract formulation of the optimization problem given in (10), let us discuss the specific choices for the electron gun shown in Figure 1. We begin the optimization procedure with a B-spline curve of degree $p = 7$ without any internal knots. This is equivalent to a simple polynomial of degree 7, however both in terms of the presented isogeometric setting, and also for later refinements, it makes sense to interpret it in the B-spline context. The curve is a reasonable compromise between design freedom, simplicity, and the desire to obtain a smooth and manufacturable solution. The control points of the initial guess are determined by a least squares fit of the original ‘flat’ design, as shown in Figure 6, and the exact parameters can be found in [56]. In order to

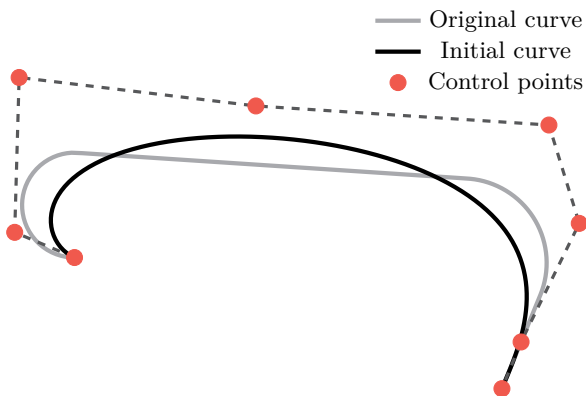


Figure 6: Original curve and the least squares fit serving as the initial shape for the optimization.

keep the overall geometry intact, the first and last control points are both fixed in their original positions over the course of the optimization.

A. Optimization results

Two successive optimization cycles are performed, as described in section IV. The first one uses a global optimization algorithm (ISRES) with a relative tolerance of 10^{-3} on the objective function, and the second utilizes a local algorithm (COBYLA) with a relative tolerance of 10^{-4} . The volume constraint is set at $V_c = 625 \text{ cm}^3$, based on the assumptions that the insulator assembly can support a maximum weight of 5 kg and a stainless steel (1.4404) electrode is used. The bounds for the admissible set can be found in [56]. The resulting shapes are shown in Figure 7. From this point onward we refer to the curve obtained via COBYLA, see Figure 7, as the optimized shape, and it will serve as the starting point for further analyses. The global optimization algorithm took about a week to find a solution satisfying our requirements, however it is possible to lower this number significantly by choosing a larger value for the tolerance or selecting to only perform a local optimization. In contrast, the local algorithm only required computation times of around 7 hours to find a sufficiently converged solution.

The electric field solutions corresponding to the original and optimized curves are depicted in Figure 5. We observe a clearly visible reduction of the maximum field strength, and in addition, the change in the electric field magnitude along the electrode appears smoother for the optimized geometry. For the solution based on the isogeometric technique, described in section III B, the open source package GEOPDES is used [46]. The B-spline space is chosen as $\mathbb{S}_{2,2}^{3,3}$ and each of the parametric do-

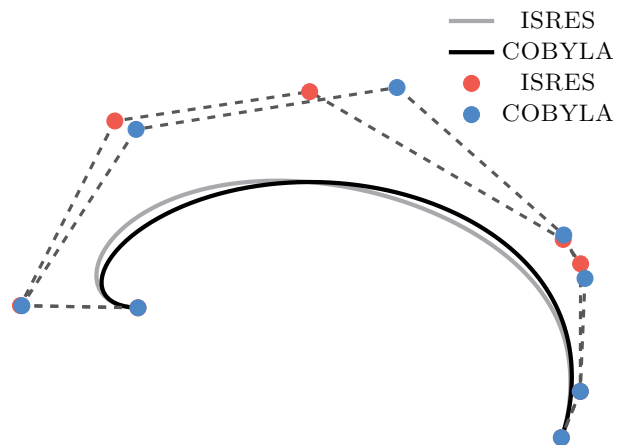


Figure 7: Curves obtained from optimizations employing ISRES and COBYLA respectively.

main, of the patches indicated in Figure 4, is divided into $n_{\text{sub}} = 16$ elements per coordinate direction using uniform knot insertion. For verification, both the original and optimized geometries are imported into CST Studio Suite 2019, and the field problem is solved using their adaptive mesh refinement with a tolerance of 10^{-4} , based on a discretization with second order tetrahedral elements. The Dirichlet boundary conditions, as marked in Figure 4, are chosen as $\Gamma_{D_0} = 0 \text{ V}$, $\Gamma_{D_1}(\mathbf{P}) = -300 \text{ kV}$, and $\Gamma_{D_2} = 1 \text{ kV}$.

The numerical values of the objective function and the volume constraint, for the original and optimized geometries respectively, are listed in Table I, where

$$E_{\text{max}}^* = \max_{\mathbf{x} \in \Omega_{\text{opt}}^{2D}(\mathbf{P})} \|\mathbf{E}_h(\mathbf{x}; \mathbf{P})\|_2$$

is introduced for brevity; \star refers to the used code. We observe a significant reduction in the maximum electric field strength, such that it falls well below the desired 10 MV m^{-1} for the optimized electrode. The volume constraint is also fulfilled at 618 cm^3 even though the initial shape had violated the requirement (630 cm^3). Finally, it can be seen that the results of our code ('IGA') and CST's EM Studio ('CST') are in good agreement.

Table I: Maximum electric field magnitude at critical points for the original and optimized geometries.

(MV m^{-1})	$E_{\text{max}}^{\text{IGA}}$	$E_{\text{max}}^{\text{CST}}$	$E_{\text{tp}}^{\text{IGA}}$	$E_{\text{c}}^{\text{IGA}}$	$E_{\text{ar}}^{\text{IGA}}$
Original	13	12.933	3.77	2.314	6.5
Optimized	9.06	9.06	4.38	2.99	5.63

Apart from the electrode, the maximum electric field strength on the cathode surface is also of interest. The numerical solution yields a value of 2.99 MV m^{-1} ($E_{\text{c}}^{\text{IGA}}$) for the optimized geometry, well below the 3.9 MV m^{-1} that are documented for the former Jefferson Lab FEL gun that was routinely operated at -320 kV [57]. This value is expected to yield a sufficiently low energy spread [58], and preliminary results are shown in section V C. A more thorough integration of a particle tracking software into the shape optimization process will allow to further improve this value.

Another important quantity is the magnitude of the electric field at the so-called triple point, where electrode, insulator, and vacuum meet. Closeups of the field surrounding the triple point are shown in Figure 5. Our simulations predict a value of 4.38 MV m^{-1} ($E_{\text{tp}}^{\text{IGA}}$) for the optimized geometry, a significant increase compared to the 3.77 MV m^{-1} for the original geometry. While the new value is still well below the safety limit, it may be necessary to further optimize the design and include additional shielding to minimize the field gradient at this critical point, as shown in [59]. Such measures could also influence the potential distribution and electric field magnitude along the outer insulator at the back of the electrode. Numerical results for these quantities can be seen

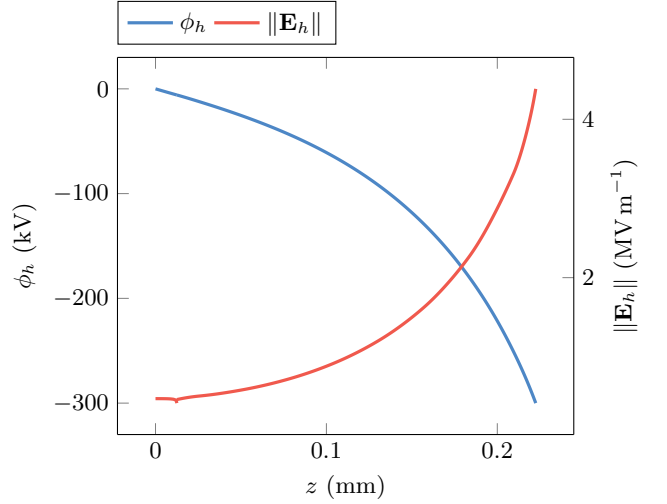


Figure 8: Potential distribution and magnitude of the electric field gradient along the outer insulator at the back of the electrode.

in Figure 8 and show a non-linear behavior. Adapting the design to linearize the field gradient along the insulator surface may improve performance and reduce the chance of electrical breakdown at high voltages [12, 60]. Lastly, the maximum value of the field gradient on the surface of the anode ring is 5.63 MV m^{-1} ($E_{\text{ar}}^{\text{IGA}}$) according to our computations. It may also be possible to further reduce this value, since the shape of the anode ring was not optimized in this work. The maximal field magnitudes, at

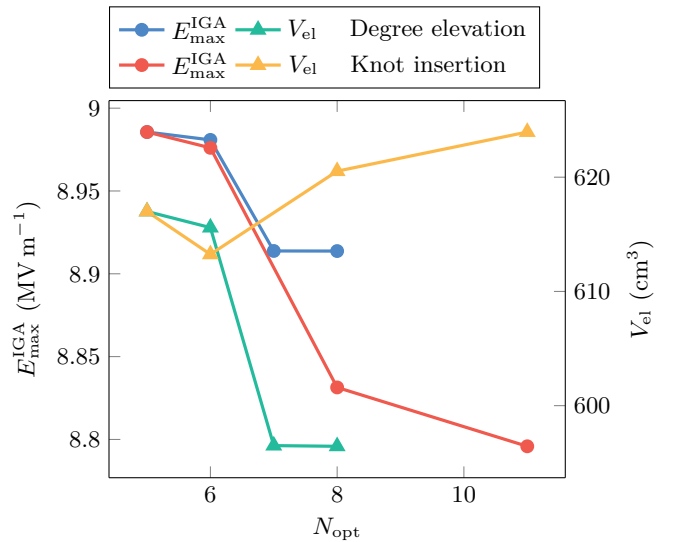


Figure 9: Convergence of maximum electric field magnitude and volume constraint with respect to curve degree and number of internal knots.

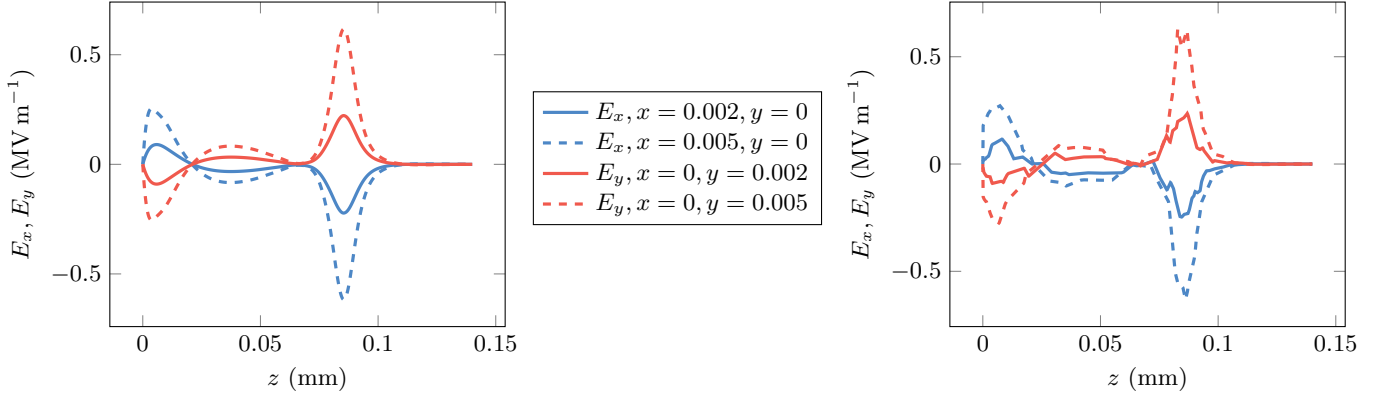


Figure 10: Comparison of electric field solutions computed using IGA (left) and linear tetrahedral finite elements (right). The fields close to the beam axis clearly showcase the advantages of IGA for obtaining smooth fields for tracking purposes.

all critical points and for both the original and optimized geometries, are listed in Table I.

We complete our study of the geometry by looking at the convergence of the optimized parameters with respect to degree elevation and knot insertion. As discussed in section II, both refinement types add additional control points to an existing curve which increases the number of degrees of freedom. In the case of knot insertion the solution space is expanded even further, since the continuity of the basis in the new knot values is reduced, thus allowing a reduced continuity of the curve. The results in terms of the maximum electric field strength and the volume of the electrode are shown in Figure 9. In the case of degree elevation, the degree of the curve is continually increased by 1, i.e., $p \in \{7, 8, 9, 10\}$. For knot insertion, the intervals of the underlying knot vector are repeatedly halved by inserting additional knots, i.e., $\Xi_0 = (\mathbf{0}_{1 \times 7}, \mathbf{1}_{1 \times 7})$, $\Xi_1 = (\mathbf{0}_{1 \times 7}, \frac{1}{2}, \mathbf{1}_{1 \times 7})$, $\Xi_2 = (\mathbf{0}_{1 \times 7}, \frac{1}{4}, \frac{1}{2}, \frac{3}{4}, \mathbf{1}_{1 \times 7})$, $\Xi_3 = (\mathbf{0}_{1 \times 7}, \frac{1}{8}, \frac{1}{4}, \frac{3}{8}, \frac{1}{2}, \frac{5}{8}, \frac{3}{4}, \frac{7}{8}, \mathbf{1}_{1 \times 7})$, while the degree is kept constant at $p = 7$. The corresponding optimization cycles are carried out with COBYLA. One can clearly observe a correlation between the number of control points N_{opt} and the quality of the solution. For this example, the solutions based upon knot insertion seem to make better use of the available volume when compared to the ones from degree elevation, however this may simply be due to a local optimum.

B. Smoothness of IGA solutions

In section I and section IIIB we already mentioned the higher global smoothness of the discrete fields when using IGA instead of classical finite elements. This is especially relevant for tracking applications, as the quality of the particle trajectories directly depends on the quality and properties of the electric field. To illustrate our

point Figure 10 shows a comparison between our IGA-based solution using GEOPDES and a linear finite element solution from CST. By E_x, E_y we denote the x - or y -component of the electric field strength respectively. We look at the field close to the beam axis and again employ CST's adaptive refinement tool with a tolerance of 10^{-4} to obtain a 'realistic' comparison. The results show a distinct difference in favor of IGA, since the unstructured mesh of the FE method, combined with the low order basis functions, leads to noisy fields.

As the shape optimization is only carried out in Ω_{opt}^{2D} , one may assume that the tracking results are not severely affected by it, and therefore we did not consider the last constraint (11) within the optimization. Nonetheless, the following section shows a preliminary investigation of the emission process and electron acceleration to ensure a solid gun performance with the optimized geometry.

C. Particle tracking results

Aside from fulfilling the previously discussed optimization criteria, the electric field should also be suitable for the initial acceleration of electrons emitted from the photocathode. In section IIIC we already introduced ASTRA and our quantities of interest. In this context, Figure 11 shows the initial macroparticle distribution in space for $N_p = 2^{11}$ particles, which was obtained from a measurement using the DataRay BeamMap2 Beam Profiler. The laser spot has an oval shape with rms radii of $r_{x,\text{rms}} = 0.41 \text{ mm}$ and $r_{y,\text{rms}} = 0.72 \text{ mm}$. The corresponding data is also available at [56]. The emission times of the particles are drawn from a normal distribution with mean 0 s and standard deviation 5 ps. This represents a practical compromise between accuracy and simplicity, however there exists extensive work on the details of the emission process and the bunch profile in time [61]. The thermal emittance, representing the minimal

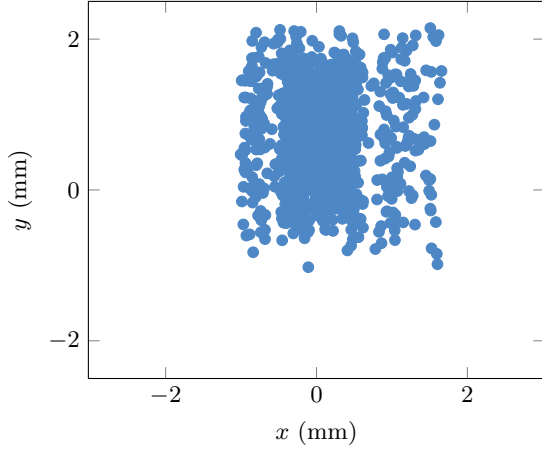


Figure 11: Initial spatial distribution of the $N_p = 2^{11}$ macroparticles to be emitted from the cathode. The positions are sampled from a measurement of the diode laser in use at Photo-CATCH.

emittance of a photoemission electron source, depends on material properties and the illuminating wavelength [62], and therefore on the photocathode material. In order to conduct a more general simulation, we thus assume the particles to have no initial momentum. The total bunch charge is estimated at 100 fC, corresponding to the planned operation of the gun at Photo-CATCH. The gun is expected to produce a continuous waveform beam with a current of 300 μ A at a repetition rate of 3 GHz, which is optimized for the operational parameters of TU Darmstadt's superconducting electron accelerator S-DALINAC [63, 64].

Table II: Relative errors in rms beam width and transverse emittance, separated by coordinate direction.

(%)	$\delta_{x_{\text{rms}}}$	$\delta_{y_{\text{rms}}}$	δ_{ϵ_x}	δ_{ϵ_y}
Initial	4.563	2.243	8.423	10.439
Refined	1.553	0.992	4.079	4.305

In addition to the already described parameters we initially choose a total of $N_p = 2^{11}$ macroparticles, a time step of about $\Delta t = 0.244$ ps for the Runge-Kutta integrator, and we set the grid for the electric field to be equidistant with $n_x = n_y = 16$ points ($\Delta x = \Delta y = 0.156$ mm) in the transverse directions and $n_z = 256$ points ($\Delta z = 0.547$ mm) in the longitudinal direction. The space charge computation is performed on a grid with $n_r = 64$ ($\Delta r = 0.039$ mm) radial and $n_l = 64$ ($\Delta l = 2.188$ mm) longitudinal cells. Remembering \mathbf{x}_{rms} as introduced in (8), we define $\bar{\mathbf{x}}_{\text{rms}}$ to be a reference solution computed with refined parameters, and similarly we take ϵ_x from (9) and define $\bar{\epsilon}_x$. More specifically, we look at two further simulations: The first uses half of the original time step Δt , twice the number of grid points

and cells, as well as double the number of macroparticles N_p . The second one is the aforementioned reference, which again halves or doubles the parameter values. We then consider errors defined by

$$\delta_{x_{\text{rms}}} = \max_{1 \leq i \leq N_z} \frac{(\mathbf{x}_{\text{rms}})_i - (\bar{\mathbf{x}}_{\text{rms}})_i}{(\bar{\mathbf{x}}_{\text{rms}})_i}$$

$$\delta_{\epsilon_x} = \max_{1 \leq i \leq N_z} \frac{(\epsilon_x)_i - (\bar{\epsilon}_x)_i}{(\bar{\epsilon}_x)_i}$$

in the computed statistical quantities with respect to the selected parameters. The corresponding numerical results are collected in Table II. We observe changes below 5 % between the reference and the first refinement step, indicating reliable results.

The computational effort for the tracking simulations is split into two parts: The creation of fieldmaps based on the numerical field solution, and the actual particle tracking procedure. For the initial parameters, the fieldmap computation took about one hour and the tracking algorithm required around ten minutes to complete a single run. Thus the fieldmap computation clearly is the bottleneck in terms of integrating particle simulations into the optimization procedure, however it may be possible to obtain sufficiently accurate maps with significantly less effort, and only verify the results afterwards using a more accurate simulation. The computation times for the refined simulations may be estimated by a linear scaling, i.e., doubling the number of longitudinal grid cells, or particles, roughly doubles the execution time as well. It should also be noted that the creation of fieldmaps is a highly parallelizable task, such that considerable speedup could be achieved by a more optimized implementation.

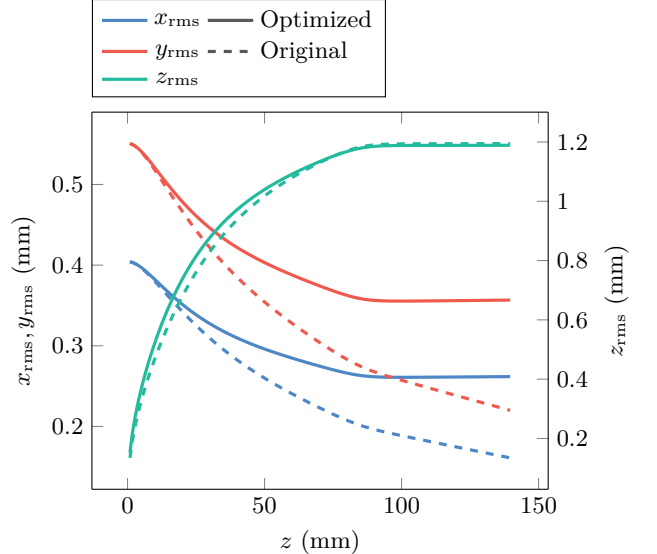


Figure 12: Rms beam widths and rms beam length for the optimized and original geometries as obtained from the simulation using ASTRA with the reference parameters.

The numerical solutions for x_{rms} and y_{rms} , interpreted as functions of z , are shown in Figure 12. Also included is the bunch length z_{rms} , which may be defined analogous to (8). It can be observed that the optimization slightly worsens these beam parameters, but not by an intolerable amount. Still, this indicates that future work could achieve even better results by also considering the shape of the electrode leading into the photocathode. Our quantities of interest, evaluated at the chamber exit, are listed in Table III. They match the values measured at operating photo-electron guns [11, 12], indicating the reliability of our simulations.

Table III: Quantities of interest for different geometries and operational parameters. All quantities are evaluated at the chamber exit.

	Optimized	Original	77 pC	77 pC, -150 kV
x_{rms} (mm)	0.258	0.161	2.146	2.648
y_{rms} (mm)	0.36	0.22	3.261	3.956
z_{rms} (mm)	1.189	1.195	12.612	22.702
ϵ_x (mrad mm)	0.108	0.116	16.786	12.967
ϵ_y (mrad mm)	0.194	0.208	36.622	27.035
ϵ_z (keV mm)	0.06	0.06	1337	1291

Aside from considering the specific parameters of the S-DALINAC, we also perform simulations based on the MESA design in use at bERLinPro. For this, we first increase the bunch charge from 100 fC to 77 pC and then reduce the bias voltage to -150 kV. The immense increase in bunch charge leads to a very visible change of the beam parameters, compare Figure 13. When also taking into account the reduced bias voltage we observe

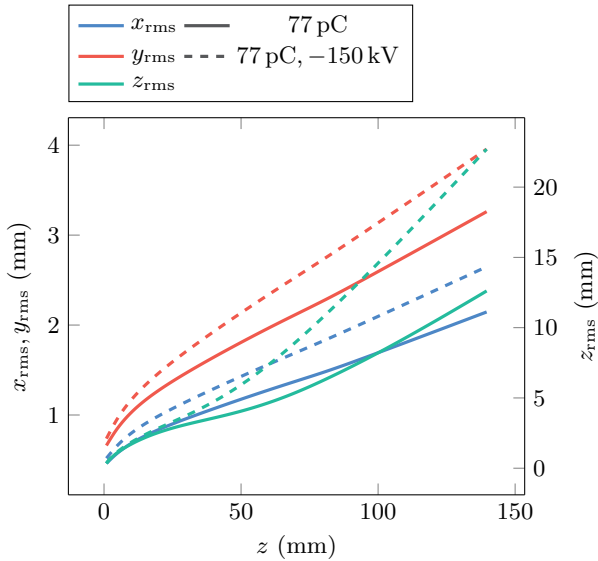


Figure 13: Rms beam widths and rms beam length as obtained from a simulation with increased bunch charge (77 pC) and reduced electrode bias voltage (-150 kV).

yet another increase, see also Table III.

Lastly, Figure 14 shows that the beam fits well inside the 20 mm aperture of the anode ring, even when considering an upscaling of the values by a factor of 10 to include a safety margin. In addition to the values collected in Table III, an rms energy spread of $\Delta E_{\text{rms}} = 48.4$ eV is observed at the chamber exit for a field strength of 2.99 MV m^{-1} on the photocathode surface at -300 kV bias voltage. Comparing these values to the 84 eV with 2.5 MV m^{-1} at -200 kV bias voltage, as reported in [58], further supports the validity of our results. It should still be possible to improve on these values, since the laser shape that was used for the simulations was unprocessed after emission from the laser diode. Moreover, the procedure presented in this work focused solely on reducing the maximum electric field strength on the electrode surface and did not include the shapes of the electrode and anode ring in the optimization. Taking their effect on the beam parameters into account could therefore provide additional improvements. As mentioned before, the initial momentum of the emitted particles needs to be included as well, which is expected to increase both rms emittance and rms energy spread. Specific optimization of the emission properties is the focus of ongoing work on the design.

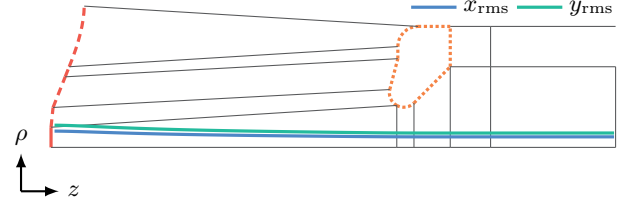


Figure 14: Rms beam widths in relation to part of the geometry. The values are scaled up by a factor of 10 to indicate that the focussing effect of the electric field is sufficiently strong.

VI. CONCLUSION AND OUTLOOK

A successful IGA-based shape optimization of a DC high-voltage photo-electron gun was performed. The maximum electric field strength of the optimized geometry was computed as 9.06 MV m^{-1} , which is well below the field emission threshold of 10 MV m^{-1} . This constitutes a reduction in the maximum field gradient by more than 25 % compared to the initial design prior to optimization. Furthermore, the optimized electrode complies with the weight and volume restrictions, and the maximum field strength on the cathode surface is determined to be 2.99 MV m^{-1} , which allows for a sufficiently low energy spread of the electron beam. The procedure was carried out for an electrode voltage of -300 kV and an anode voltage of 1 kV, with a fixed anode cathode gap of

80 mm. Some beam parameters of the resulting geometry, namely the rms beam widths and length, the normalized transverse and longitudinal rms beam emittances, and the rms energy spread were investigated using the particle tracking software ASTRA. Preliminary results were found to be in agreement with measurements at operating guns and exhibited values suitable for the setup at Photo-CATCH.

The work presented here solely focused on the optimization of the maximum electric field strength. In the future, the same procedure may be applied to the entire electrode, and the anode ring also, optimizing both their shapes and the anode-cathode distance. This includes fully coupling the shape optimization with a particle tracking software as well, to optimize the emission properties of the gun and investigate the influence of the

electrode geometry on beam properties for ERL-typical bunch charges of 100 pC and above. In this context, it could also prove useful to allow for a direct evaluation of the spline basis functions within the tracking code, to make full use of the increased accuracy and smoothness without sacrificing computational efficiency.

ACKNOWLEDGMENTS

The authors gratefully acknowledge the fruitful discussions with Simon Friederich, Yuliya Fritzsche and Steffen Schmid. M. Herbert and J. Enders acknowledge support by the Deutsche Forschungsgemeinschaft (DFG) - Projektnummer 264883531 (GRK 2128 “AccelencE”) and the German BMBF (05H18RDRB1).

-
- [1] C. K. Sinclair, DC photoemission electron guns as ERL sources, *Nuclear Instruments and Methods in Physics Research Section A: Accelerators, Spectrometers, Detectors and Associated Equipment* **557**, 69 (2006), Energy Recovering Linacs 2005.
 - [2] T. Rao *et al.*, Photocathodes for the energy recovery linacs, *Nuclear Instruments and Methods in Physics Research Section A: Accelerators, Spectrometers, Detectors and Associated Equipment* **557**, 124 (2006), energy Recovering Linacs 2005.
 - [3] J. Maxson, I. Bazarov, B. Dunham, J. Dobbins, X. Liu, and K. Smolenski, Design, conditioning, and performance of a high voltage, high brightness DC photoelectron gun with variable gap, *Review of Scientific Instruments* **85**, 093306 (2014).
 - [4] C. K. Sinclair, P. A. Adderley, B. M. Dunham, J. C. Hansknecht, P. Hartmann, M. Poelker, J. S. Price, P. M. Rutt, W. J. Schneider, and M. Steigerwald, Development of a high average current polarized electron source with long cathode operational lifetime, *Phys. Rev. ST Accel. Beams* **10**, 023501 (2007).
 - [5] J. R. Pierce, Rectilinear electron flow in beams, *Journal of Applied Physics* **11**, 548 (1940), <https://doi.org/10.1063/1.1712815>.
 - [6] D. E. Radley, The theory of the pierce type electron gun, *Journal of Electronics and Control* **4**, 125 (1958), <https://doi.org/10.1080/00207215808953831>.
 - [7] I. V. Bazarov and C. K. Sinclair, Multivariate optimization of a high brightness dc gun photoinjector, *Phys. Rev. ST Accel. Beams* **8**, 10.1103/PhysRevSTAB.8.034202 (2005).
 - [8] I. V. Bazarov, A. Kim, M. N. Lakshmanan, and J. M. Maxson, Comparison of dc and superconducting rf photoemission guns for high brightness high average current beam production, *Phys. Rev. ST Accel. Beams* **14**, 10.1103/PhysRevSTAB.14.072001 (2011).
 - [9] J. Grames, R. Suleiman, P. A. Adderley, J. Clark, J. Hansknecht, D. Machie, M. Poelker, and M. L. Stutzman, Charge and fluence lifetime measurements of a DC high voltage gaas photogun at high average current, *Phys. Rev. ST Accel. Beams* **14**, 043501 (2011).
 - [10] M. Breidenbach, M. Foss, J. Hodgson, A. Kulikov, A. Odian, G. Putallaz, H. Rogers, R. Schindler, K. Skarpaas, and M. Zolotarev, An inverted-geometry, high voltage polarized electron gun with UHV load lock, *Nuclear Instruments and Methods in Physics Research Section A: Accelerators, Spectrometers, Detectors and Associated Equipment* **350**, 1 (1994).
 - [11] Y. Poltoratska *et al.*, Status and recent developments at the polarized-electron injector of the superconducting Darmstadt electron linear accelerator S-DALINAC, *Journal of Physics: Conference Series* **298**, 012002 (2011).
 - [12] C. Hernandez-Garcia *et al.*, Compact -300 kV dc inverted insulator photogun with biased anode and alkali-antimonide photocathode, *Phys. Rev. Accel. Beams* **22**, 113401 (2019).
 - [13] N. Nishimori, R. Nagai, S. Matsuba, R. Hajima, M. Yamamoto, Y. Honda, T. Miyajima, H. Iijima, M. Kuriki, and M. Kuwahara, Experimental investigation of an optimum configuration for a high-voltage photoemission gun for operation at ≥ 500 kV, *Phys. Rev. ST Accel. Beams* **17**, 053401 (2014).
 - [14] P. A. Adderley, J. Clark, J. Grames, J. Hansknecht, K. Surles-Law, D. Machie, M. Poelker, M. L. Stutzman, and R. Suleiman, Load-locked DC high voltage GaAs photogun with an inverted-geometry ceramic insulator, *Phys. Rev. ST Accel. Beams* **13**, 010101 (2010).
 - [15] C. K. Sinclair, H. F. Dylla, T. L. Siggins, L. Wu, and T. J. Venhaus, Dramatic reduction of field emission from large area electrodes by plasma-source ion implantation, in *Proc. 2001 Particle Accelerator Conference (PAC'01), Chicago, IL, USA, June 18-22, 2001*, Particle Accelerator Conference (IEEE Xplore, 2001) pp. 610–612.
 - [16] M. BastaniNejad *et al.*, Evaluation of niobium as candidate electrode material for DC high voltage photoelectron guns, *Phys. Rev. ST Accel. Beams* **15**, 083502 (2012).
 - [17] F. Furuta *et al.*, Reduction of field emission dark current for high-field gradient electron gun by using a molybdenum cathode and titanium anode, *Nuclear Instruments and Methods in Physics Research Section A: Accelerators, Spectrometers, Detectors and Associated Equipment* **538**, 33 (2005).

- [18] N. Kurichyanil, J. Enders, Y. Fritzsche, and M. Wagner, A test system for optimizing quantum efficiency and dark lifetime of GaAs photocathodes, *Journal of Instrumentation* **14** (08), P08025.
- [19] M. Herbert, J. Enders, Y. Fritzsche, N. Kurichyanil, and V. Wende, Inverted geometry photo-electron gun research and development at TU Darmstadt, in *Proc. 9th International Particle Accelerator Conference (IPAC'18), Vancouver, BC, Canada, April 29-May 4, 2018*, International Particle Accelerator Conference No. 9 (JACoW Publishing, Geneva, Switzerland, 2018) pp. 4545–4547.
- [20] M. Hinze, R. Pinnau, M. Ulbrich, and S. Ulbrich, *Optimization with PDE Constraints*, Mathematical Modelling: Theory and Applications (Springer, 2008).
- [21] P. Monk, *Finite Element Methods for Maxwell's Equations* (Oxford University Press, 2003).
- [22] P. Di Barba, *Multiobjective Shape Design in Electricity and Magnetism*, Lecture Notes in Electrical Engineering (Springer, 2010).
- [23] B. M. Lewis, H. T. Tran, M. E. Read, and R. Ives, Design of an electron gun using computer optimization, *IEEE Transactions on Plasma Science* **32**, 1242 (2004).
- [24] W. Jiang, Y. Luo, R. Yan, and S. Wang, Genetic algorithm-based shape optimization of modulating anode for magnetron injection gun with low velocity spread, *IEEE Transactions on Electron Devices* **62**, 2657 (2015).
- [25] C. Ribton and W. Balachandran, Development of an evolutionary algorithm for design of electron guns for material processing, in *7th International Joint Conference on Computational Intelligence (IJCCI 2015)*, Vol. 1 (IEEE, 2015) pp. 138–148.
- [26] G. Stancari and J. Edelen, Optimization of field at cathode with python wrapper and SPIFFE, <https://cdcvns.fnal.gov/redmine/projects/mcmillan-electron-gun/wiki> (2017).
- [27] E. T. Tulu, U. van Rienen, and A. Arnold, Systematic study of multipactor suppression techniques for a superconducting rf gun, *Phys. Rev. Accel. Beams* **21**, 113402 (2018).
- [28] C. De Boor, On calculating with B-splines, *Journal of Approximation theory* **6**, 50 (1972).
- [29] L. Piegl and W. Tiller, *The NURBS Book*, 2nd ed. (Springer, 1997).
- [30] P. T. Boggs, A. Althsuler, A. R. Larzelere, E. J. Walsh, R. L. Clay, and M. F. Hardwick, *DART system analysis*, Technical Report (Sandia National Laboratories, 2005).
- [31] K. Halbach, Superfish? a computer program for evaluation of rf cavities with cylindrical symmetry, *Particle Accelerators* **7**, 213 (1976).
- [32] Dassault Systèmes, *CST STUDIO SUITE 2019* (2019).
- [33] E. Gjonaj, W. Ackermann, T. Lau, T. Weiland, and M. Dohlus, Coupler kicks in the third harmonic module for the XFEL, in *Proceedings of PAC09* (PAC09, 2009).
- [34] J. A. Cottrell, T. J. R. Hughes, and Y. Bazilevs, *Isogeometric Analysis: Toward Integration of CAD and FEA* (Wiley, 2009).
- [35] D. M. Nguyen, A. Evgrafov, J. Gravesen, and D. Lahaye, Iso-geometric shape optimization of magnetic density separators, *COMPEL: The International Journal for Computation and Mathematics in Electrical and Electronic Engineering* **33**, 1416 (2014).
- [36] A. Pels, Z. Bontinck, J. Corno, H. De Gersem, and S. Schöps, Optimization of a Stern-Gerlach magnet by magnetic field-circuit coupling and isogeometric analysis, *IEEE Transactions on Magnetics* **51**, 10.1109/TMAG.2015.2462806 (2015).
- [37] M. Merkel, P. Gangl, and S. Schöps, *Shape Optimization of Rotating Electric Machines using Isogeometric Analysis*, Preprint arxiv:1908.06009 (Cornell University, 2019).
- [38] Z. Bontinck, J. Corno, H. De Gersem, S. Kurz, A. Pels, S. Schöps, F. Wolf, C. de Falco, J. Dölz, R. Vázquez, and U. Römer, Recent advances of isogeometric analysis in computational electromagnetics, *International Computation Society Newsletter* **24** (2017).
- [39] L. Piegl and W. Tiller, Curve and surface constructions using rational B-splines, *Computer-Aided Design* **19**, 485 (1987).
- [40] E. Cohen, R. F. Riesenfeld, and G. Elber, *Geometric Modeling with Splines: An Introduction* (CRC Press, 2001).
- [41] C. de Boor, *A Practical Guide to Splines*, rev. ed., Applied Mathematical Sciences, Vol. 27 (Springer, 2001).
- [42] M. Spink, D. Claxton, C. de Falco, and R. Vázquez, *NURBS Package* (2017).
- [43] J. D. Jackson, *Classical Electrodynamics*, 3rd ed. (Wiley & Sons, 1998).
- [44] A. Buffa, R. H. Vázquez, G. Sangalli, and L. B. a. da Veiga, Approximation estimates for isogeometric spaces in multipatch geometries, *Numerical Methods for Partial Differential Equations* **31**, 422 (2015).
- [45] A. Simona, L. Bonaventura, C. de Falco, and S. Schöps, IsoGeometric approximations for electromagnetic problems in axisymmetric domains, *Computer Methods in Applied Mechanics and Engineering* **369**, 113211 (2020).
- [46] R. Vázquez, A new design for the implementation of isogeometric analysis in Octave and Matlab: GeoPDEs 3.0, *Comput. Math. Appl.* **72**, 523 (2016).
- [47] K. Floettmann, *A Space Charge Tracking Algorithm Version 3.2*, Deutsches Elektronen-Synchrotron DESY (2017).
- [48] R. W. Hockney and J. W. Eastwood, *Computer simulation using particles* (crc Press, 1988).
- [49] C. K. Birdsall and A. B. Langdon, *Plasma physics via computer simulation* (CRC press, 2004).
- [50] Y. N. Grigoryev, V. A. Vshivkov, and M. P. Fedoruk, *Numerical "particle-in-cell" Methods: Theory and Applications* (Walter de Gruyter, 2012).
- [51] A. Simona, L. Bonaventura, T. Pognat, and B. Dalena, High order time integrators for the simulation of charged particle motion in magnetic quadrupoles, *Communications in Computational Physics* **239**, 33 (2019).
- [52] K. Floettmann, Some basic features of the beam emittance, *Phys. Rev. ST Accel. Beams* **6**, 034202 (2003).
- [53] T. P. Runarsson and Xin Yao, Search biases in constrained evolutionary optimization, *IEEE Transactions on Systems, Man, and Cybernetics, Part C (Applications and Reviews)* **35**, 233 (2005).
- [54] M. J. D. Powell, A direct search optimization method that models the objective and constraint functions by linear interpolation, in *Advances in Optimization and Numerical Analysis*, edited by S. Gomez and J.-P. Hennart (Springer Netherlands, Dordrecht, 1994) pp. 51–67.
- [55] S. G. Johnson, *The NLOpt nonlinear-optimization package Version 2.6.2* (2020).
- [56] P. Förster, S. Schöps, and A. Simona, *EgunOpt* (2020), <https://github.com/temf/EgunOpt>.
- [57] T. Siggins, C. Sinclair, C. Bohn, D. Bullard, D. Douglas, A. Grippo, J. Gubeli, G. A. Krafft, and B. Yunn, Perfor-

- mance of a DC GaAs photocathode gun for the Jefferson lab FEL, Nuclear Instruments and Methods in Physics Research A **475**, 549 (2001).
- [58] S. Friederich and K. Aulenbacher, Test electron source for increased brightness emission by near band gap photoemission, in *Proc. 6th International Particle Accelerator Conference (IPAC'15), Richmond, VA, USA, May 3-8, 2015*, International Particle Accelerator Conference No. 6 (JACoW, Geneva, Switzerland, 2015) pp. 1512–1514, <https://doi.org/10.18429/JACoW-IPAC2015-TUPWA044>.
- [59] G. Palacios-Serrano, F. Hannon, C. Hernandez-Garcia, M. Poelker, and H. Baumgart, Electrostatic design and conditioning of a triple point junction shield for a -200 kV DC high voltage photogun, Review of Scientific Instruments **89**, 104703 (2018), <https://doi.org/10.1063/1.5048700>.
- [60] C. Hernandez-Garcia, M. Poelker, and J. Hansknecht, High voltage studies of inverted-geometry ceramic insulators for a 350 kV DC polarized electron gun, IEEE Transactions on Dielectrics and Electrical Insulation **23**, 418 (2016).
- [61] M. Espig, J. Enders, Y. Fritzsche, and M. Wagner, Investigation of pulsed spin polarized electron beams at the S-DALINAC, in *Proceedings of XVth International Workshop on Polarized Sources, Targets, and Polarimetry — PoS(PSTP2013)*, Vol. 182 (2014) p. 059.
- [62] I. V. Bazarov, B. M. Dunham, Y. Li, X. Liu, D. G. Ouzounov, C. K. Sinclair, F. Hannon, and T. Miyajima, Thermal emittance and response time measurements of negative electron affinity photocathodes, Journal of Applied Physics **103**, 054901 (2008), <https://doi.org/10.1063/1.2838209>.
- [63] A. Richter, Operational experience at the S-DALINAC (Inst. of Physics Publ, Bristol, Philadelphia, 1996) ersch. ebenf. als: Technische Universität Darmstadt, Institut für Kernphysik: IKDA; 96/17.
- [64] N. Pietralla, The institute of nuclear physics at the TU Darmstadt, Nuclear Physics News **28**, 4 (2018).